Surface & Coatings Technology 512 (2025) 132414

Contents lists available at ScienceDirect

Surface & Coatings Technology

journal homepage: www.elsevier.com/locate/surfcoat

Dual-layer TiO_2/PDMS composite coating on Ti6Al4V titanium alloy with superhydrophobicity and enhanced corrosion resistance and mechanical stability

Yinghe Ma [a], Yonghui Hu [a], Zhen Yu [a], Zhihui Cai [b], Wenjian Zheng [a], Jianguo Yang [a,*], Paul K. Chu [c,*]

[a] Institute of Process Equipment and Control Engineering, College of Mechanical Engineering, Zhejiang University of Technology, Hangzhou, China
[b] Wenzhou Special Equipment Inspection & Science Research Institute, Wenzhou, China
[c] Department of Physics, Department of Materials Science and Engineering, Department of Biomedical Engineering, City University of Hong Kong, Kowloon, Hong Kong, China

ARTICLE INFO

Keywords:
Titanium alloy
Micro-arc oxidation
Polydimethylsiloxane
Superhydrophobicity
Corrosion resistance

ABSTRACT

A dual-layer protective coating with superhydrophobicity and enhanced corrosion resistance and stability is prepared on titanium alloy by *in situ* formation of micro-protrusions by micro-arc oxidation (MAO) in a Si—P electrolyte and high-temperature vapor deposition of polydimethylsiloxane (PDMS). The superhydrophobic composite coating exhibits a water surface contact angle of 166.2°. Electrochemical corrosion tests in 3.5 wt% NaCl solution reveal that the corrosion current density of the superhydrophobic surface is three orders of magnitude lower than that of the MAO-treated surface alone, giving rise to a corrosion inhibition efficiency of 99.88 %. Mechanistic analysis reveals that the composite coating impedes electrolyte penetration due to the multiscale roughness and PDMS layer with a low surface energy. Furthermore, the coating maintains the robust mechanical stability during abrasion tests and exhibits self-cleaning properties, boding well for applications in harsh environments.

1. Introduction

Titanium alloys with excellent specific strength, low density, and biocompatibility are used in many areas such as marine, aerospace, and biomedical components [1–4]. However, severe friction and wear conditions and long-term exposure to corrosive media can impair the surface integrity and cause corrosion failure [5]. Hence, surface treatment techniques such as electroplating, plasma spraying, electrodeposition, and micro-arc oxidation (MAO) have been proposed to improve the surface properties [6–9]. In micro-arc oxidation, an oxide film is grown *in situ* on the Ti alloy in an electrolyte [10–12] to improve the corrosion resistance and stability [13–15]. However, micro-arc oxidation is normally carried out in a high-temperature and high-pressure environment, which inevitably produces pores and cracks, which allow corrosive liquids to penetrate and corrode the substrate [16–19].

Researchers have tried to improve the corrosion resistance of micro-arc oxidized coatings [20,21]. For example, Wang et al. [22] have used the LSR technique to modulate the laser energy density to reduce the number of pores, and Chen et al. [23] have added MoS_2 particles to the electrolyte to improve the corrosion resistance. Wang et al. [24] have introduced ZrO_2 and Y_2O_3 nanoparticles during MAO to reduce cracking by exploiting the dislocation pinning effect at the semi-coherent interface, and the best corrosion resistance is achieved using a concentration of 1.2 mol%/L Y^{3+}. Buyuksungur et al. [25] have prepared TiO_2 coatings with good corrosion resistance and antimicrobial properties by regulating the Zn concentrations in the MAO coatings.

Natural lotus leaves have superhydrophobic and self-cleaning properties on account of the micro- and nanotopography and low surface energy, and consequently, nature-inspired superhydrophobic coatings have been prepared to improve anti-icing, anti-fouling, and corrosion resistance [26–28] on stainless steel, carbon steel, copper, magnesium, aluminum, titanium, and other alloys [29,30]. Zou et al. [31] have deposited cerium hexadecanoate coatings on aluminum alloy by micro-arc oxidation and electrodeposition to improve the corrosion resistance and self-cleaning properties. Zhang et al. [32] have used PDMS and EP epoxy resin as binders and HDTMS-modified Al_2O_3 nanoparticles as

* Corresponding authors.
E-mail addresses: yangjg@zjut.edu.cn (J. Yang), paul.chu@cityu.edu.hk (P.K. Chu).

https://doi.org/10.1016/j.surfcoat.2025.132414
Received 30 April 2025; Received in revised form 6 June 2025; Accepted 17 June 2025
Available online 18 June 2025

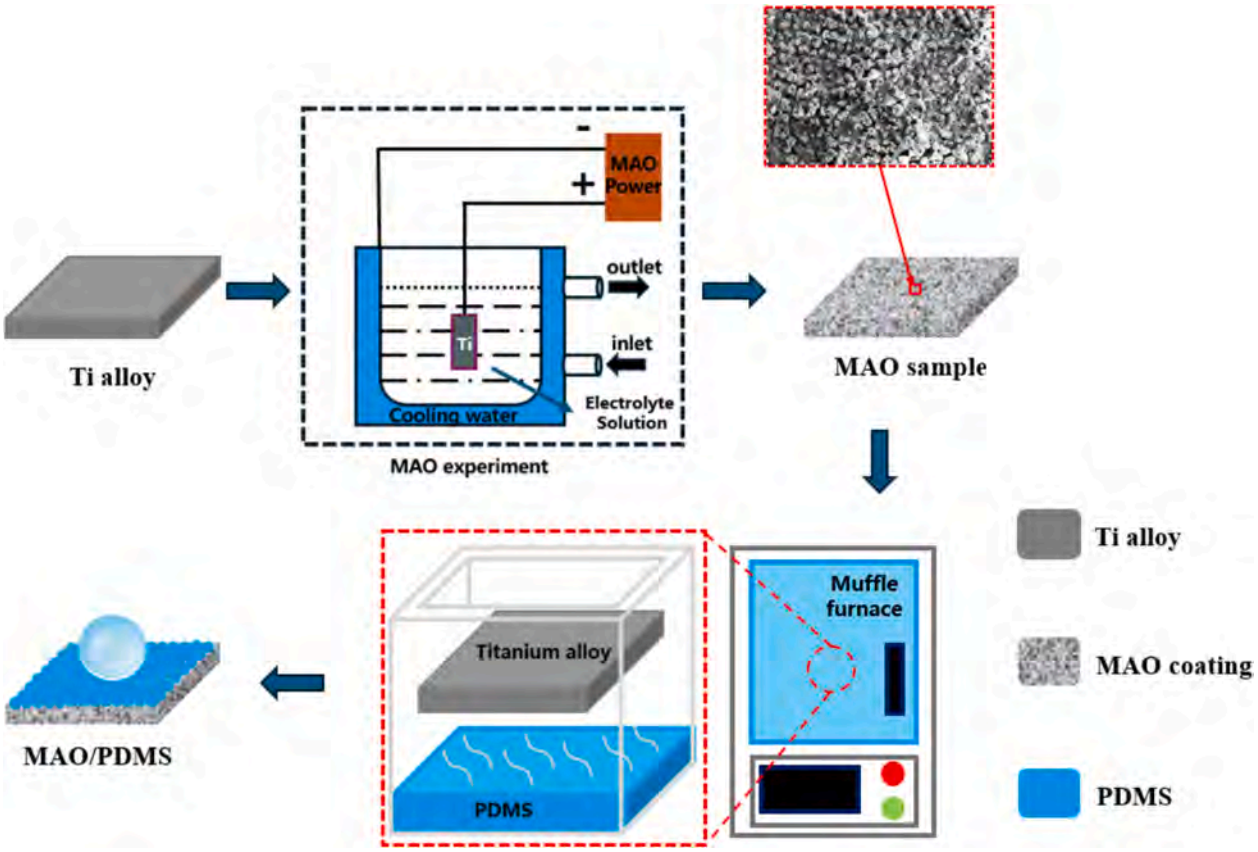

Fig. 1. Schematic of the fabrication process of the superhydrophobic samples.

fillers for Q235 carbon steel in air spraying, resulting in an improvement of seven orders of magnitude in the charge transfer resistance (R_{ct}) in comparison with the carbon steel substrate. Xu et al. [33] have used nanosecond laser technology to etch micro/nano-patterns on titanium alloys. MAO is used for anti-corrosion, and the grafting of hydrophobic surface groups leads to surface superhydrophobicity and mechanical stability. Patterned surfaces etched by laser nanosecond etching can provide protection for low surface energy materials with good mechanical stability; however, patterned surfaces can also be constructed in one step by micro-arc oxidation. Wang et al. [34] used a novel plasma-enhanced high temperature liquid-phase-assisted oxidation and cross-linking (PHLOC) technique to prepare porous coatings different from those of conventional micro-arc oxidation in Si-P-K electrolyte, with papillae-like structures and remarkable layered surface textures. In PDMS vapor deposition studies, Ye et al. [35] used chemical nickel plating combined with electrochemical etching to construct a micro-nano-structure on a copper substrate, and then obtained a composite coating by vapor deposition of PDMS, which increased the self-corrosion current density by four orders of magnitude compared to that of the copper substrate. Zhang et al. [36] constructed a black ceramic coating on a magnesium alloy surface combined with vapor deposition to achieve photo-thermal superhydrophobicity, and investigated its dynamic icing and melting behavior. In addition, there are few studies on the preparation of superhydrophobic surfaces by combining the vapor deposition technique with the micro-arc oxidation technique, which is of some research value.

In addition, by adding nanoparticles can make the coating have good electrochemical stability and mechanical properties, Shibli and Chacko [37] introduced TiO_2 nanoparticles in phosphate coatings making the coating thicker, better corrosion resistance as well as barrier protection properties. Kathavate and Deshpande [38] were able to improve the electrochemical and nano-mechanical properties of electrochemically deposited phosphate coatings by incorporating TiO_2 nanoparticles and ZnO nanoparticles in aqueous phosphate baths, followed by cost-effective annealing treatments. However, the tribological properties of the composite coatings after the introduction of nanoparticles have not been investigated.

Herein, inspired by the *in-situ* construction of papillae-patterned surfaces by microarc oxidation, hierarchical and multi-scale micro/nanostructures are fabricated on the Ti6Al4V titanium alloy by MAO and chemical vapor deposition (CVD). MAO enhances the wear protection, and PDMS is introduced by CVD to form a dual coating with excellent mechanical stability, self-cleaning properties, and corrosion resistance. Friction and wear tests were performed on MAO-Ti and MAO/PDMS surfaces to investigate the effect of nanoparticles produced by vapor deposition on the tribological properties of the coatings.

2. Experimental details

2.1. Materials

Industrial titanium alloy (Ti6Al4V, 2 mm thick) was used as the substrate. Sodium silicate, potassium hydroxide, sodium hexametaphosphate, and anhydrous ethanol were purchased from Sinopharm, and sodium chloride was purchased from Xilong Group. The polydimethylsiloxane (PDMS) prepolymer (Sylgard 184A) was bought from Dow Corning, and 400# and 1000# sandpapers were obtained from 3 M China. The reagents were analytical grade and used without purification.

2.2. Sample preparation

The alkaline electrolyte contained sodium silicate (15 g/L), sodium hexametaphosphate (10 g/L), and potassium hydroxide (2 g/L) in

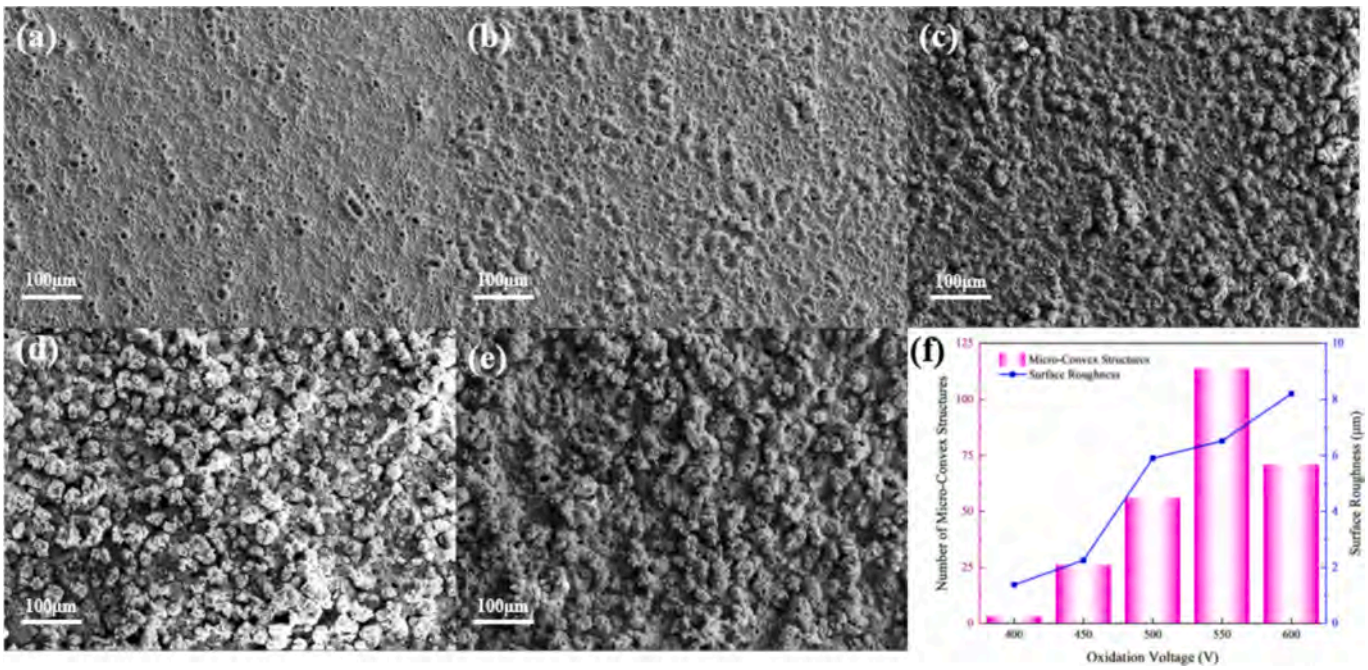

Fig. 2. SEM of different voltages sample: (a) 400 V, (b) 450 V, (c) 500 V, (d) 550 V, (e) 600 V; (f) the surface roughness and the number of micro-convex structure at different voltages.

deionized water. The Ti6Al4V titanium plates (20 mm × 20 mm × 2 mm) were ground with *SiC* sandpapers from 400# to 1000# and cleaned ultrasonically in anhydrous ethanol and acetone for 10 min each. They underwent MAO in an electrolyte (FL-MAO30B), with the titanium alloy being the anode and the stainless-steel drum as the cathode. Cooling water was circulated to prevent the electrolyte from overheating. MAO was conducted using the following parameters: pulse frequency of 600 Hz, duty cycle of 9 %, reaction time of 10 min in the constant voltage mode, and oxidation voltage of 550 V. After the process was completed, ultrasonic cleaning was performed in anhydrous ethanol, dried, and sealed for future use.

The polydimethylsiloxane (3 g, without added hardener) prepolymer was placed in a quartz crucible, and the MAO sample was positioned about 3 cm from the PDMS prepolymer. The quartz crucible was placed in a muffle furnace and heated at a rate of 10 °C/min to 400 °C for 2 h to form the superhydrophobic coating. The preparation process is shown in Fig. 1.

2.3. Self-cleaning and stability assessment

The self-cleaning performance is examined by using silica sand as the contaminating medium, placing the sample on a slide with a tilt angle of about 20°, placing a certain amount of silica sand on the sample surface, and using a dropper to take one milliliter of distilled water, with the mouth of the dropper about 2 cm from the surface of the sample, and dropping drops of the taken distilled water on the sample surface to examine its self-cleaning performance. The mechanical stability was evaluated by tape stripping and sandpaper abrasion using 3M898 tape on the sample surface and a load of 100 g for 30 s. The tape was pulled quickly until it detached completely. For each 10 peeling cycles, the surface angle was measured at 3 different locations. Sandpaper abrasion was performed by placing the sample on 2000# sandpaper under loads of 100 g, 50 g, and 20 g. The abraded distance was 100 mm, and the surface angle was again measured from 3 different positions.

2.4. Friction experiment

The Abrasion experimenter (Rtec-Instruments, MFT-5000) was used to conduct the friction experiment. In order to investigate the effect of nanoparticles produced by vapor deposition on the tribological properties of coatings, MAO-Ti and MAO/PDMS sample were subjected to friction tests. The selected friction sub-material was bearing steel balls (G10) with a diameter of 6 mm. The experimental load was 0.3 N and the speed was 1 cm/s. The experiment was repeated three times under non-lubricated conditions, respectively, and each friction test lasted for 10 min. At the end of the friction experiment, the friction profile was photographed.

2.5. Characterization

The water contact angle was measured on an optical contact angle meter using a 5 μL droplet of distilled water. The chemical properties and composition of the samples were determined by Fourier transform infrared (FTIR) spectroscopy (Thermo Fisher Scientific Nicolet iS20). X-ray diffractometer (XRD, X' Pert PRO) was utilized to analyze the phase composition of the coatings. The MAO-Ti and MAO/PDMS samples were placed in a salt spray corrosion test chamber (DCTC1200PNW) for accelerated corrosion testing under the following conditions: 5 wt% NaCl solution, 35 °C. A 3D surface profiler (KEYENCE VK-X150) was used to photograph the three-dimensional shape of the sample and measure the arithmetic mean surface roughness (Sa). The electrochemical properties were determined on an electrochemical workstation (CorrTest CS350H) in a 3.5 wt% NaCl solution using the three-electrode configuration comprising the working electrode (sample), auxiliary electrode (platinum sheet), and reference electrode (saturated potassium chloride). Prior to the electrochemical test, the samples were immersed in 3.5 % NaCl for 30 min for stabilization according to the open circuit potential (OCP). Relative to the OCP, the polarization parameters were: scanning rate of 10 mV/s, starting voltage of −1.5 mV, and terminating voltage of 2 mV. The corrosion current density (i_{corr}) was calculated by Tafel extrapolation. The electrochemical impedance spectra (EIS) were acquired in the frequency range between 10^5 Hz and 10^{-2} Hz with an AC amplitude of 10 mV. The Zview software was adopted to analyze and fit the electrochemical impedance spectra. Experiments were performed in triplicate on all samples to ensure reproducibility.

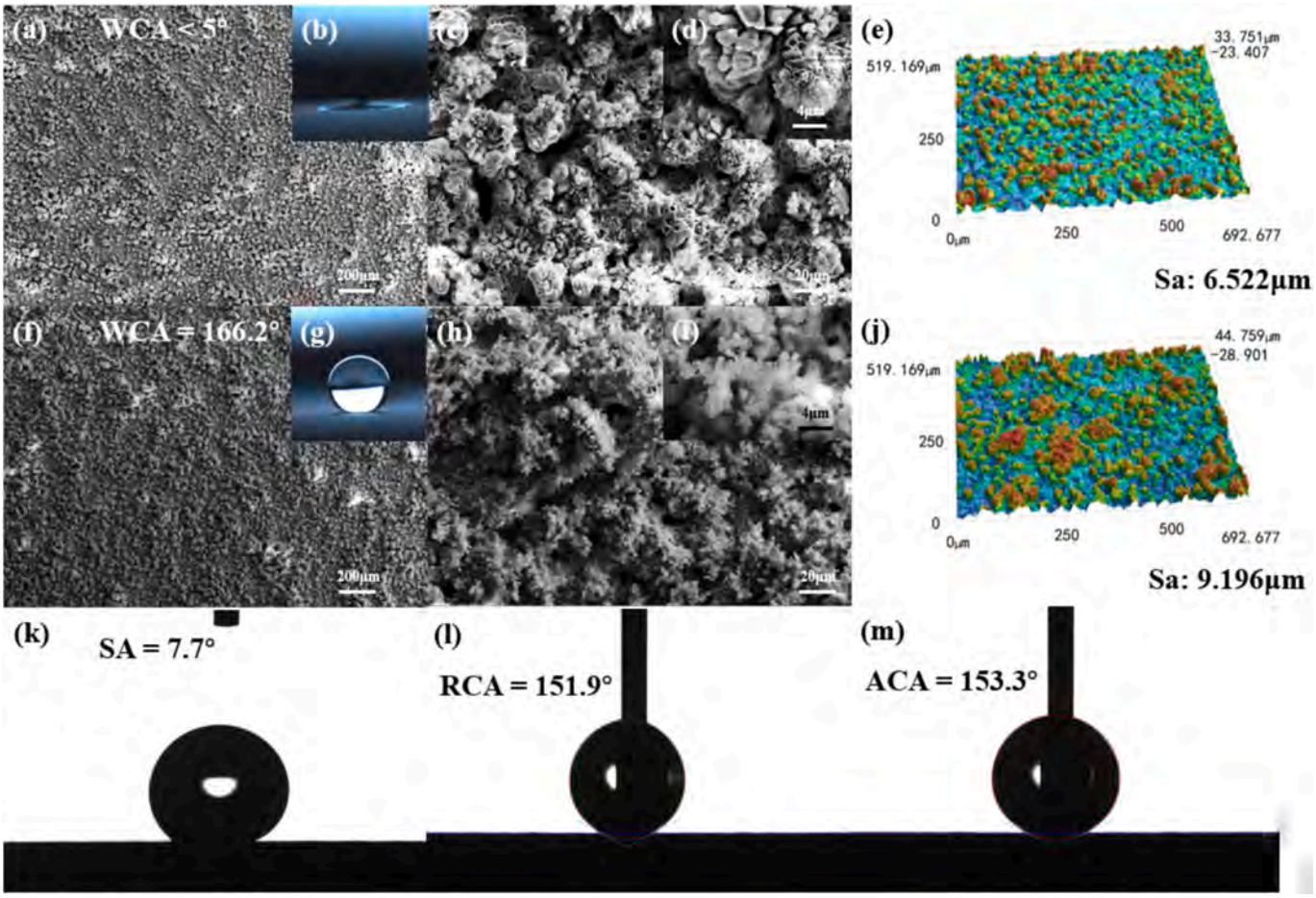

Fig. 3. SEM images: (a, c, d) MAO-Ti and (f, h, i) MAO/PDMS at different magnifications. The insets in (b) and (g) are the static contact angles of water droplets (~5 μL) on MAO-Ti and MAO/PDMS. 3D surface topographies of (e) MAO-Ti and (j) MAO/PDMS; Sliding angle(k), receding contact angles (l) and advancing contact angles (m) of MAO/PDMS.

3. Results and discussion

3.1. Surface morphology and wettability

Fig. 2 shows the surface morphology of the coatings at different voltages as well as the statistics of the number of surface micro-convex structures and the surface roughness due to the application of different voltages, from which it can be seen that the coatings are typical porous structures at oxidation voltages of 400 V and 450 V (Fig. 2(a)(b)), and the coatings are accompanied by violent discharge phenomena at 450 V, and the coatings have a more obvious bulge. When the oxidizing voltage is 500 V (Fig. 2(c)), the coating has a porous structure and a micro-convex structure due to the voltage increase. This micro-convex structure is mainly due to the micro-arc oxidation reaction process, intense spark discharge on the surface of the titanium alloy produces many discharge micro-channels, spark discharge when a single discharge point instantaneous temperature of up to 5000 K, a large number of molten oxides accompanied by discharge micro-channels at high temperatures and pressures like a volcanic eruption gushing out. Molten oxides in contact with the electrolyte in the process of temperature plummet, coupled with the same area through multiple discharges, the melt repeatedly erupt and solidify, thus forming this micro-bump structure, one of the conditions for obtaining superhydrophobic coatings is to have a certain degree of roughness, so that the coating is able to capture the air. This provides the possibility of building superhydrophobic coatings at a later stage [39]. At an oxidizing voltage of 550 V (Fig. 2(d)), the micro-convex structures on the surface of the coating are more uniform, and the number of micro-convex structures is the highest at this point, reaching 114 (Fig. 2(f)). However, at an oxidizing voltage of 600 V (Fig. 2(e)), the original micro-convex structures become disordered due to overburning and collapsing of the structures caused by the excessively high discharge energy. The surface roughness of the coating increases with the increase of oxidizing voltage, and at an oxidizing voltage of 400 V, its surface roughness is 1.375 μm, and its surface is relatively smooth. When the oxidizing voltage is 450 V, 500 V, 550 V and 600 V, its surface roughness is 2.255 μm, 5.902 μm, 6.522 μm and 8.214 μm respectively.

Fig. 3 shows the SEM images and static contact angles of the MAO-Ti and MAO/PDMS coatings. Fig. 3(a) shows the morphology of the titanium alloy after MAO, revealing that the surface of MAO-Ti has microbumps and microcracks besides nanoscale bumps and holes in the discharge channels, as shown in Fig. 3(c). The static contact angle of the coating after MAO is <5° due to the presence of surface hydroxyl hydrophilic groups.

Fig. 3(e), (g), and (h) depicts the surface morphology of the MAO/PDMS coating. Compared to the MAO sample, there are discharge holes and microbumps. The spherical PDMS nanoparticles (NPs) are 50 nm to 500 nm in size, and the static contact angle is 166.2°. PDMS is unstable at 400 °C, leading to volatilization when the MAO is heated at 400 °C for 2 h. The PDMS NPs with low surface energy and rough surface topography with microbumps lead to the formation of the hierarchical multiscale micro-nanostructure. Fig. 3(i) and (j) shows the 3D images of the two coatings. The roughness of MAO-Ti after the single MAO process is 6.522 μm, whereas that of MAO/PDMS after CVD increases to 9.196 μm.

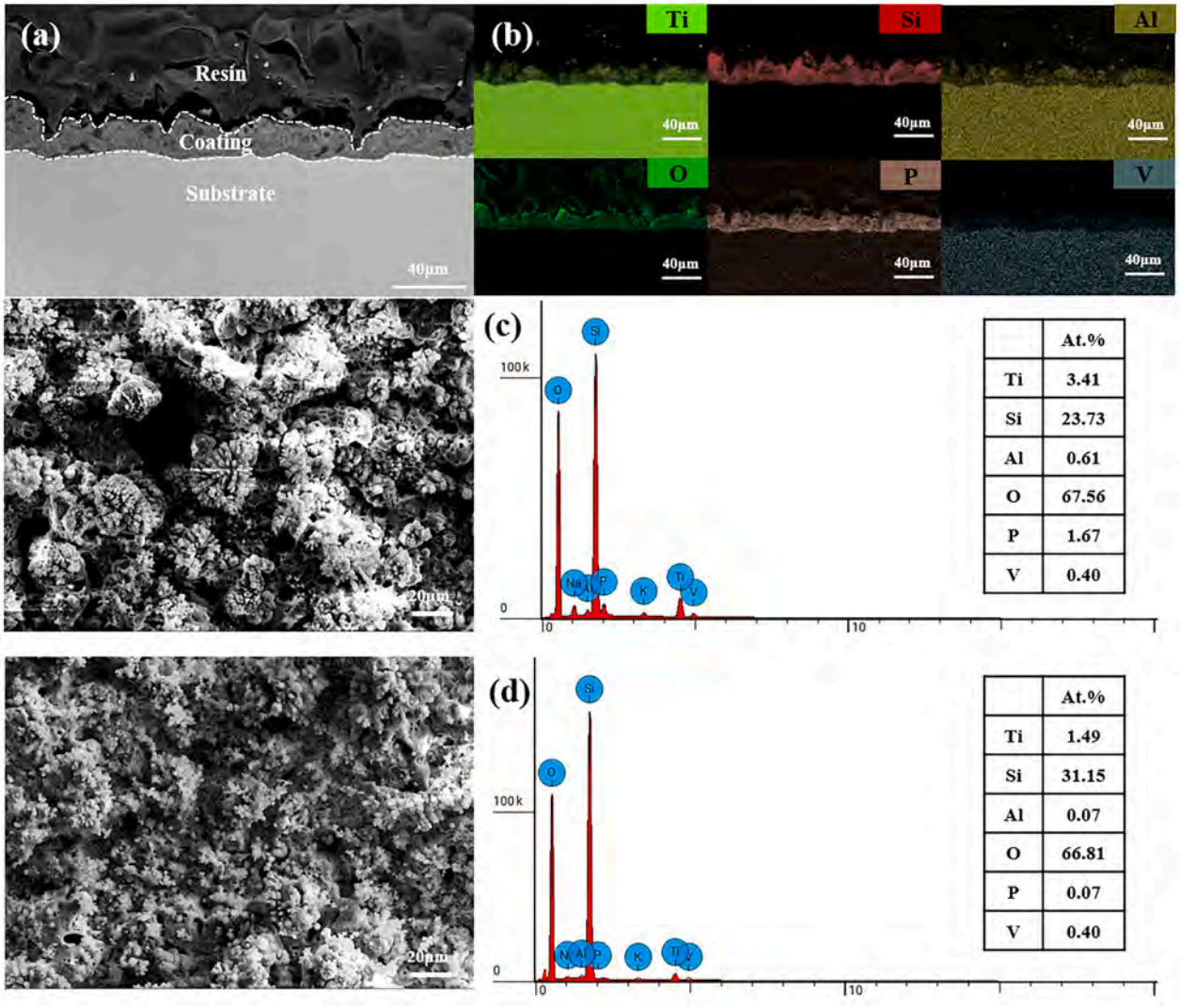

Fig. 4. Cross-section images of MAO/PDMS coating and EDS results; (a) cross-section images, (b) mapping results of Ti, Si, Al, O, P and V, (c) surface elements composition of MAO-Ti and (d) surface elements composition of MAO/PDMS.

Fig. 3(k)(l)(m) shows the rolling angle, receding angle and advancing angle of MAO/PDMS, respectively, and the rolling angle of this surface is 7.7°, so the surface has excellent self-cleaning performance. The receding angle is 151.9°, and the superhydrophobic performance is still maintained when the droplet shrinks, and the advancing angle is 153.3°, and the advancing and receding angles numerically always satisfy the theoretical range of superhydrophobic surfaces, and the corresponding hysteresis angle is 1.4°, and the hysteresis angle data indicate that the chemical distribution of the micro-nano-structures of the PDMS-modified surface of the MAO/PDMS is homogeneous. The reason that the static contact angle is larger than the advancing angle is due to the localized rupture of the air film caused by the pinning of the contact line during droplet expansion, which leads to a numerical decrease in the advancing angle.

The incomplete spreading of droplets can be explained by the Cassie-Baxter model [40], in which the surface wettability depends on the surface roughness and chemical state, as shown in the following [41,42]:

$$\cos\theta_r = f_1\cos\theta - f_2 \quad (1)$$

where θ_r is the static contact angle of the MAO/PDMS coating, θ is the static contact angle of the titanium alloy substrate surface, and f_1 and f_2 are the water-solid and water-air interfacial volume fractions, respectively ($f_1 + f_2 = 1$). The static contact angle (θ) of the titanium alloy is 80.7°, and the static contact angle (θ_r) of the MAO/PDMS coating is 166.2°. The estimated f_2 of MAO/PDMS is 0.975, showing that air occupies about 97.5 % of the contact area between the droplet and the superhydrophobic coating. It is noted that this dual surface treatment process gives rise to superior hydrophobicity compared to other polydimethylsiloxane (PDMS)-modified coatings reported in the literature. As shown in Fig. 3(f), the static contact angle of the MAO/PDMS coating prepared is 166.2°, which is a significant improvement compared to previous studies. For instance, Ye et al., [35] have used chemical nickel plating combined with electrochemical etching to construct a micro-nanostructure on a Cu substrate showing a contact angle of 158.5°, and Zhang et al. [36] have prepared a coating with a contact angle of 156.0° by MAO in conjunction with vapor-phase deposition of PDMS on the AZ31 magnesium alloy.

3.2. *Elemental analysis*

Fig. 4(a) shows the cross-sectional microscopic morphology of the sample. The coating consists of a dense inner layer and a porous outer layer. The interface between the coating and the substrate is relatively clear, due to the *in situ* growth of the MAO coating on the substrate. Fig. 4(b) shows that the cross-section of the MAO/PDMS coating contains Ti, Si, Al, V, O, and P. Ti, Al, and V originate from the Ti substrate, P

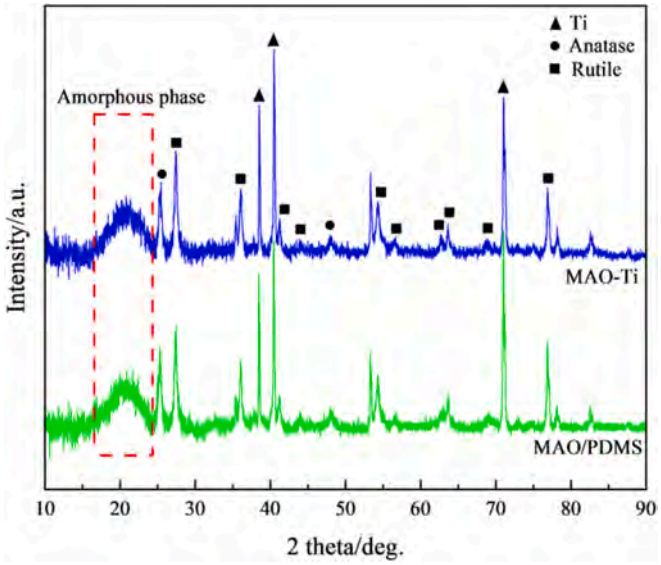

Fig. 5. XRD patterns of MAO-Ti and MAO/PDMS.

comes from the electrolyte, and Si and O are from the electrolyte and partly from the nanoparticles deposited on the surface of the coating after PDMS incorporation. Fig. 4(c) and (d) shows the surface elemental surface scans of MAO/PDMS and MAO-Ti, respectively, and the elemental Si content on the surface of MAO-Ti reaches 23.73 % due to the participation of silicate ions in the electrolyte along with the electric field force in the coating reaction (Fig. 4(c)). It is noteworthy that the elemental Si content on the MAO/PDMS surface is higher than that on MAO-Ti in Fig. 4(d), where the elemental Si content reaches 31.15 %, indicating that the nanoparticles volatilized and deposited on MAO-Ti by PDMS have a high Si content.

3.3. Chemical composition

Fig. 5 shows the XRD images of MAO-Ti and MAO/PDMS, revealing titanium with rutile and anatase phases shown by diffraction peaks in the range of 10–25°, indicating that an amorphous phase is generated in the coating. The coating contains a large amount of Si, indicating that the broad diffraction peak is amorphous SiO_2 [11,43,44]. Silicate ions formed by the hydrolysis of sodium silicate in the electrolyte move to the surface of the anode under the electric field, and the temperature and pressure of the discharge channel of 2×10^4 K and 100 MPa enable the electrolyte to enter the coating under these conditions. At the same time, the oxide melted in the high-temperature reaction cools rapidly during contact with the electrolyte, thus inhibiting nucleation and growth, so that SiO_2 is amorphous. MAO/PDMS shows broad peaks indicative of amorphous SiO_2 [45]. It is conjectured that the nanoparticles on the surface contain amorphous SiO_2 phases. XRD reveals an overlap between 10 and 25° due to the MAO-Ti substrate. Therefore, MAO/PDMS does not show significant differences compared to MAO-Ti.

The surface functional groups on MAO-Ti, original PDMS, and MAO/PDMS are analyzed by FT-IR (Fig. 6). In the FT-IR spectra of PDMS, peaks 2961 cm^{-1}, 1256 cm^{-1}, and 844 cm^{-1} correspond to the C—H asymmetric stretching vibration in -CH_3, the bending vibration of -CH_3, and the stretching vibration of -CH_3, respectively, and the symmetric stretching vibration of Si-O-Si is observed at peaks 804 cm^{-1} and 1010 cm^{-1} The presence of antisymmetric bending vibrations in CH_3 at 1450 cm^{-1} as well as 1410 cm^{-1} and the presence of two small shoulder peaks at peaks 844 cm^{-1} and 865 cm^{-1} are attributed to antisymmetric and symmetric vibrations of Si-CH_3 [46]. The peaks at 1062 cm^{-1} and 799 cm^{-1} of MAO-Ti correspond to Si-O-Si derived from the conversion of titanium into SiO_2 during MAO in the electrolyte. Compared to MAO-Ti, The three newly appeared peaks in the FT-IR spectrum of MAO/PDMS coating: 2972 cm^{-1} peak, 1404 cm^{-1} peak, 1273 cm^{-1} peak and 842 cm^{-1} peak, which are consistent with the PDMS elastomer, indicate that there is no obvious structural change in the thin layer of PDMS

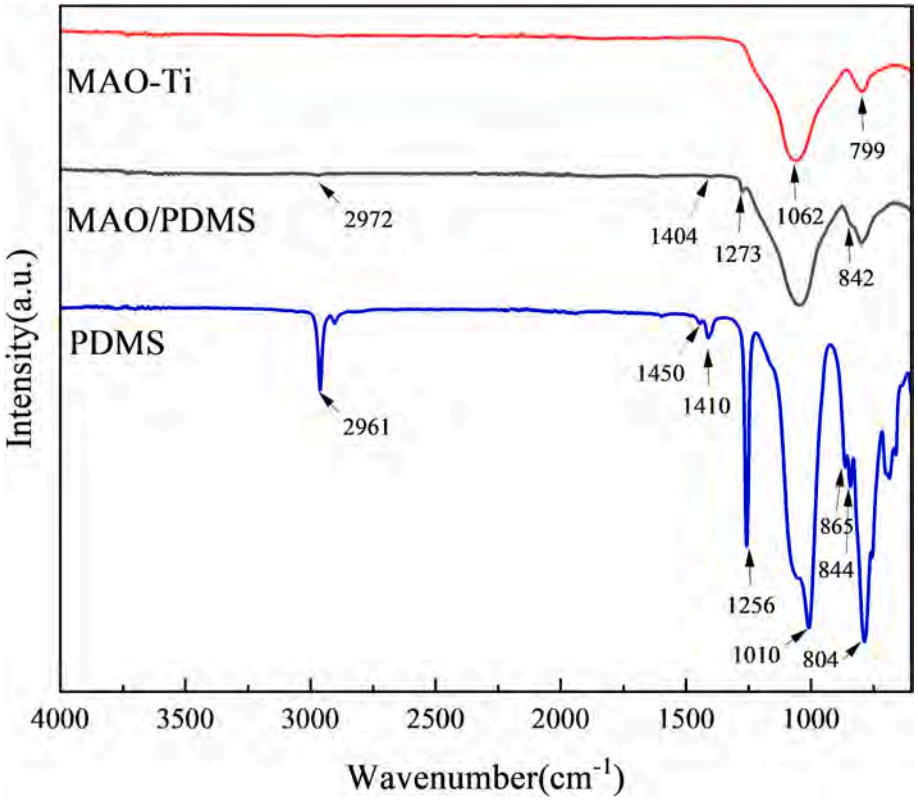

Fig. 6. FTIR spectra of MAO-Ti, Original PDMS, and MAO/PDMS.

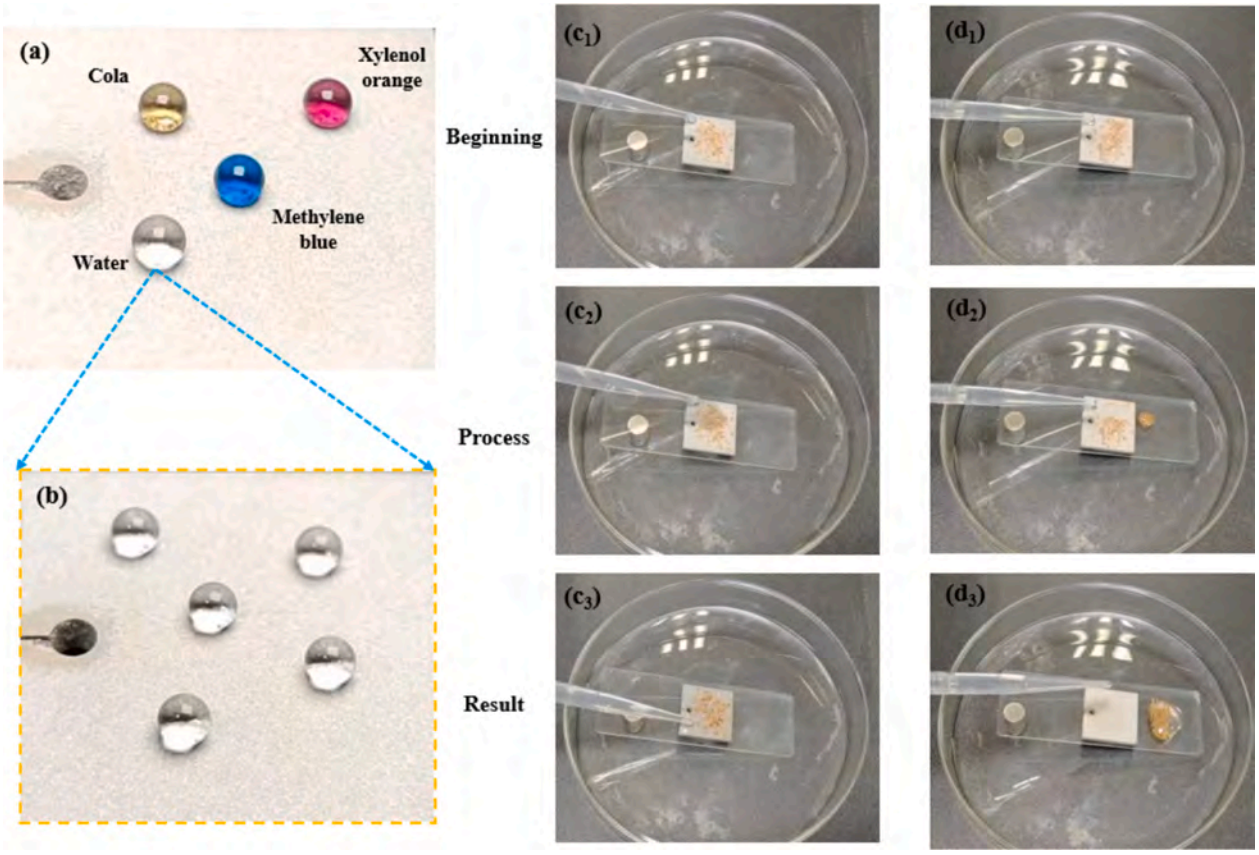

Fig. 7. Self-cleaning tests of the MAO/PDMS surface: (a, b) images of the superhydrophobic surface with various solutions (Cola, Water, Xylenol orange, and Methylene blue) and self-cleaning experiments on MAO-Ti (c_1–c_3) and MAO/PDMS (d_1–d_3). (For interpretation of the references to colour in this figure legend, the reader is referred to the web version of this article.)

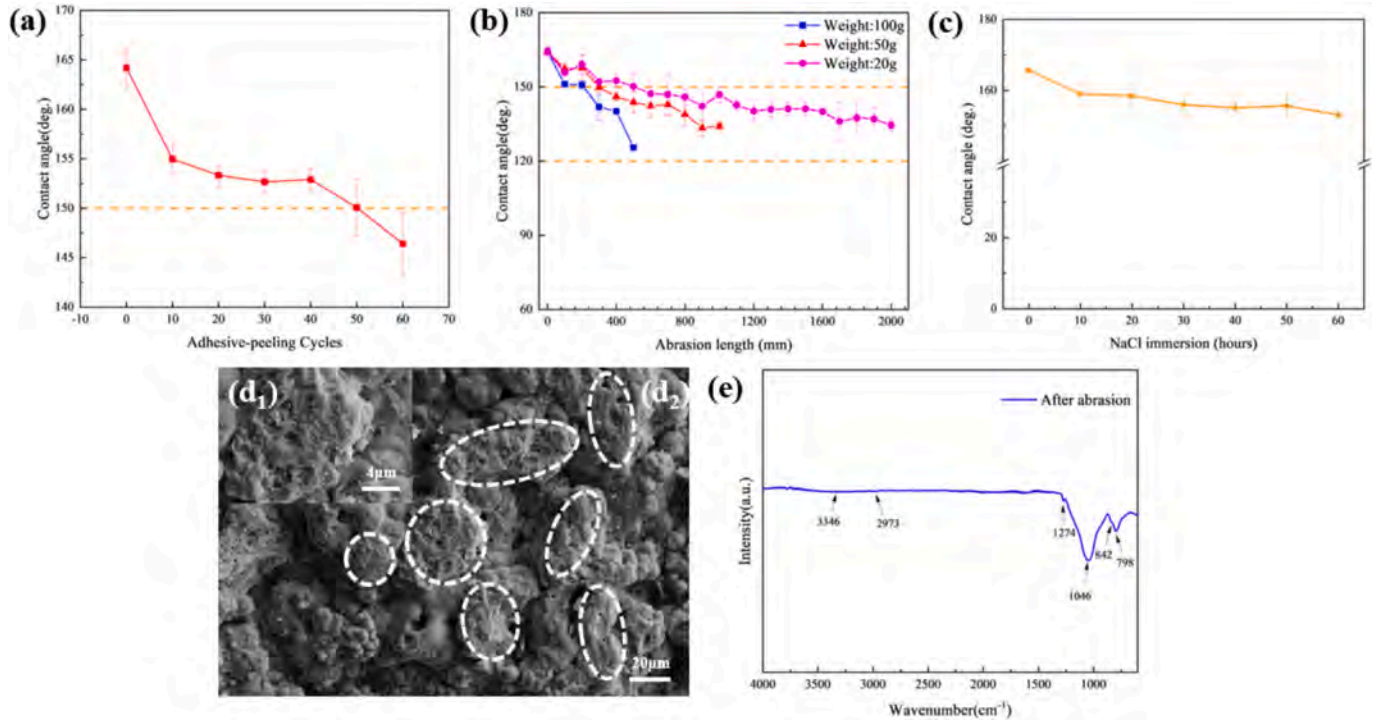

Fig. 8. Abrasion and adhesive-peeling experiments: water contact angles after (a) different peeling cycles and (b) different friction length; immersion test in 3.5 wt% NaCl solution: water contact angles after (c) different immersion times; SEM image for an abrasion distance of 2000 mm under a load of 20 g (d_1, d_2) and FT-IR spectrum after abrasion for 2000 mm (e).

nanoparticles deposited by high-temperature volatilization. The FTIR peaks from MAO/PDMS still show the -CH_3 group compared to the pristine PDMS, but the intensity is lower because during the pyrolysis of PDMS, -CH_3 is removed. The PDMS-derived silica nanoparticles connect with each other to gradually form the Si-O-Si film with residual -CH_3 groups, and the -CH_3 groups are enriched on the surface to form a low-surface-energy monomolecular layer [47,48], leading to super-hydrophobicity. The peaks of -CH_3 bending in Si-CH_3 and -CH_3 stretching in Si-CH_3 arise from PDMS pyrolysis. The results demonstrate that the nanoparticles deposited on the surface are SiO_2.

3.4. Self-cleaning and stability

The self-cleaning performance of MAO-Ti and MAO/PDMS is studied using four different droplets of deionized water, cola, methylene blue, and dimethylphenol orange. The droplets are nearly spherical ($\theta > 150°$), and the contact angles increase due to the superhydrophobic surfaces. The dye-containing solutions (methylene blue and dimethylphenol orange) and cola droplets do not spread or penetrate, suggesting repulsive effects, as shown in Fig. 7(a) and (b). Silica particles with a size of 500 μm are used as surface contaminants, and the self-cleaning efficiency is investigated by dropping deionized water onto the surface through a 2 ml dropper. On the MAO surface, owing to the hydroxyl hydrophilic groups, the droplets spread quickly, while the sand particles infiltrate and attach to the surface, indicating that the conventional MAO lacks the repelling ability (Fig. 7c_1–c_3). However, on the superhydrophobic surface, the droplets roll on the surface inclined at 20°, during which the sand particles are encapsulated and completely detach from the coating (Fig. 7d_1–d_3), efficient self-cleaning through the low-adhesion force effect (Cassie-Baxter state). This self-cleaning effect is consistent with the MAO/PDMS low hysteresis angle results. This result is attributed to the superhydrophobic modification of the surface, the inability of liquid droplets to penetrate into the micropores of the coating, the formation of a solid-liquid-gas interface, and the kinetic energy of the rolling droplets. The factors are sufficient to overcome the weak van der Waals forces between the sand particles and the surface for contaminant removal.

In order to evaluate the adhesion stability of superhydrophobic surfaces, the MAO-Ti superhydrophobic coating with PDMS is subjected to cyclic peeling by the tape peeling method. Fig. 8(a) shows that the coating remains superhydrophobic after 50 peeling cycles, with the contact angle being above 150°. However, after the 60th peeling cycle, the contact angle decreases to <150°. This phenomenon indicates the formation of a mechanical anchor between the MAO microbulge structure and PDMS NPs with strong bonding between them. The partial detachment of the layer of PDMS NPs after the 60th peeling cycle exposes the micro and nanostructures and increases the surface energy, thus shifting the wettability to the Wenzel-Cassie hybrid state.

To further investigate the anti-wear performance of the coatings, the superhydrophobic surfaces are placed and moved on 2000 grit sandpaper under loads of 100 g, 50 g, and 20 g. The contact angle changes are monitored at 100 mm intervals. As shown in Fig. 8(b), a larger load (100 g) accelerates the mechanical damage of the surface micro-nanostructures, leading to the wear of the PDMS layer and the micro-bumps on the MAO substrate, thereby causing the hydrophobicity to degrade more rapidly. At a smaller load (20 g), the wear rate decreases, and the coating maintains partial hydrophobicity ($\theta > 120°$) after a longer wear distance. Fig. 8(d) shows the microscopic morphology after a wear distance of 2000 mm. After the hydrophobic region is subjected to mechanical wear, the area of the hydrophilic region increases, resulting in a larger solid-liquid contact area, and the hydrophobic angle tends to decrease. Fig. 8(e) shows the FTIR spectra after wear. The -CH_3 methyl hydrophobic groups are still present at 2973 cm^{-1}, 1274 cm^{-1}, and 842 cm^{-1}, and Si-OH groups are present at 3346 cm^{-1} due to the exposure of the basal hydrophilic region by mechanical wear. PDMS molecules remain on the MAO microstructure after mechanical abrasion, and the MAO structure is not completely destroyed.

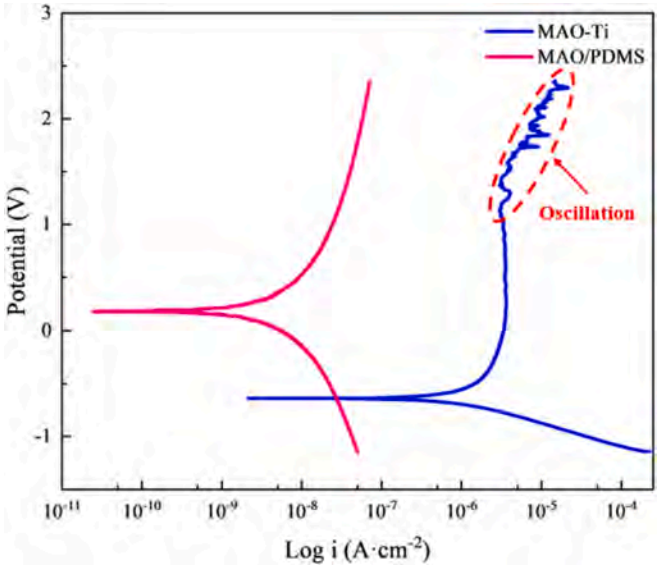

Fig. 9. Polarization curves of MAO-Ti and MAO/PDMS.

Table 1
Fitted results of the potentiodynamic polarization curves of MAO-Ti and MAO/PDMS in the 3.5 % NaCl solution.

Coatings	E_{corr}/V	β_a/(mV·dec^{-1})	$-\beta_c$/(mV·dec^{-1})	I_{corr}(A/cm^2)	R_p/(Ω·cm^2)
MAO-Ti	−0.638	1070.5	266.23	1.37E−6	6.75E7
MAO/PDMS	0.184	314.62	313.3	1.62E−9	4.21E10

Since the inherent fragility of the structure is susceptible to damage by the variable environment, the long-term stability of the coating in corrosive media needs to be examined. In this paper, 3.5 % NaCl solution is used as the corrosive substance, and it can be seen from Fig. 8(c) that after a long time of exposure to the corrosive substance, the MAO/PDMS still has good water repellency, and this contact angle is up to >150°. This wettability shows a gradual decrease, a phenomenon that indicates that the low surface energy molecules in the superhydrophobic coating are damaged with the prolongation of the immersion time. The reason for the decrease in the wettability of the coating in corrosive media is mainly due to the desorption of hydrophobic molecules on the surface due to certain chemical reactions, such as hydrolysis of chemical interfacial bonds and breaking of chemical bonds, and the exposure of defective areas of PDMS nanoparticles at the interface between the coating/corrosive media to corrosive media, which leads to structural disruption and the loss of hydrophobic functional groups [49]. The results show that MAO/PDMS superhydrophobic coatings with strong chemical interfaces are not susceptible to similar structural damage and functional group failure, and have long-term chemical stability.

3.5. Corrosion resistance

The corrosion resistance and corrosion inhibition efficiency are analyzed by the polarization curves acquired in 3.5 wt% NaCl (Fig. 9), and Table 1 shows the corrosion parameters obtained by Tafel curve fitting. The corrosion potential is the result of the dynamic equilibrium between the anodic and cathodic reactions in a corrosive medium. Compared to MAO-Ti, the self-corrosion potential of MAO/PDMS exhibits a positive shift, while the MAO-Ti current density oscillates as the corrosion potential rises, possibly due to the nucleation of unstable craters in the naturally passivated film and subsequent repassivation

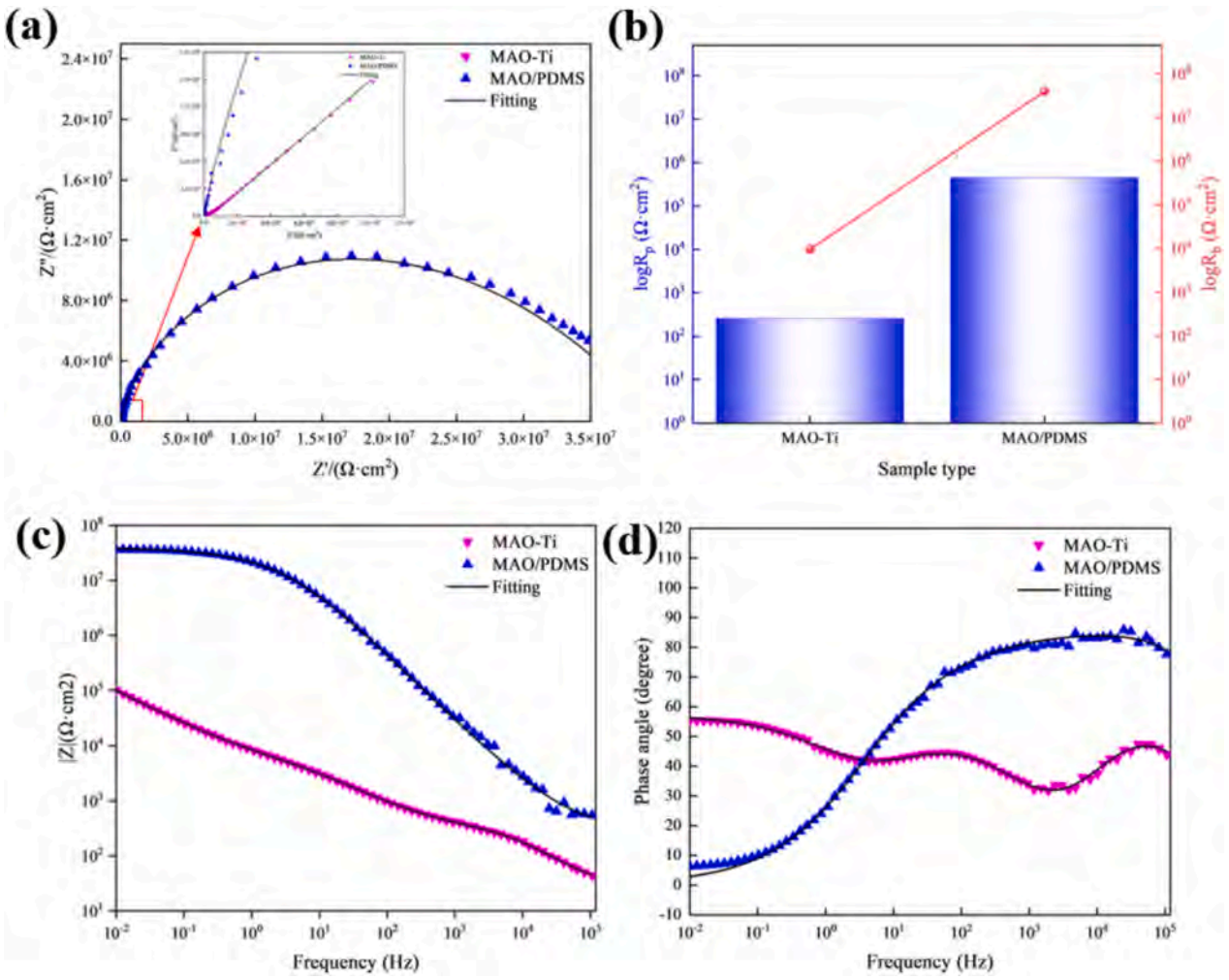

Fig. 10. (a) Nyquist plots; (b) porous layer resistance (R_p) and dense layer resistance (R_d); (c, d) bode plots in 3.5 wt% NaCl.

[15,53]. However, there is no current density oscillation for MAO/PDMS, indicating that the coating tends to passivate thermodynamically, and the corrosion tendency is reduced. It is because the inert nanoparticles of PDMS cover the active sites above the MAO coating to form a super-hydrophobic layer, and the infiltration of Cl^- ions along the pores and micro-cracks is blocked. In addition, the self-corrosion current density of MAO/PDMS (1.62×10^{-9} A/cm^2) is three orders of magnitude less than that of MAO (1.37×10^{-6} A/cm^2), attributable to the ease of corrosion of Cl^- in contact with the substrate through micropores and microchannels generated by the discharge on MAO-Ti. However, the air layer on MAO/PDMS forms a barrier against Cl^- ions to mitigate corrosion.

The corrosion inhibition rate (η) quantifies the protective performance as shown in the following [50]:

$$\eta\% = \frac{i^0_{corr} - i_{corr}}{i^0_{corr}} \times 100 \quad (2)$$

where i^0_{corr} represents the corrosion current density of the MAO coating, and i_{corr} is the corrosion current density of the MAO/PDMS coating. The corrosion inhibition efficiency of MAO/PDMS is as high as 99.88 % relative to the MAO coating. In addition, the polarization resistance quantifies the resistance against charge transfer between the metal surface and the corrosive fluid as expressed below [51]:

$$R_p = \frac{\beta_a \beta_c}{2.303(\beta_a + \beta_c) i_{corr}} \quad (3)$$

The cathodic Tafel slope (β_c) and anodic Tafel slope (β_a) are shown in Table 1, and R_p of MAO/PDMS is improved.

Electrochemical impedance spectroscopy is conducted to evaluate the corrosion resistance and behavior. Fig. 10 shows the corrosion behavior of MAO-Ti and MAO/PDMS. Generally, in the Nyquist plot, the semicircular arc diameter is proportional to the corrosion resistance of the sample. MAO-Ti exhibits three capacitance loops: the smallest one at 3.84 kHz, the middle one between 3.84 kHz and 1.7176 Hz, and a diffusion arc in the low-frequency region. The high-frequency region, middle portion, and low-frequency region are associated with the porous layer, the dense layer [52], and diffusion control [53], respectively. The porous structure in the MAO coating allows the corrosive fluid to pass through and come into contact with the substrate. The MAO/PDMS coating shows two orders of magnitude higher impedance modulus in the low-frequency region (0.01 Hz) than the MAO coating and possesses the largest arc tolerance with good corrosion shielding (Fig. 10(a)), indicating that very few electrons pass through the dense layer to reach the substrate. Fig. 10(b) shows the porous layer resistance and dense layer resistance of MAO-Ti and MAO/PDMS. The MAO/PDMS porous layer resistance increases by three orders of magnitude compared to MAO-Ti, and the dense layer resistance increases by three orders of magnitude at the same time. Hence, the porous layer is a good physical barrier because the PDMS NPs block a large number of pores and create an air layer [54]. As shown in Fig. 10(c) and (d), the impedance modulus of MAO/PDMS is significantly higher than that of MAO-Ti in the full-frequency band. The impedance modulus at 0.01 Hz increases by two orders of magnitude compared with MAO-Ti, and the phase angle of

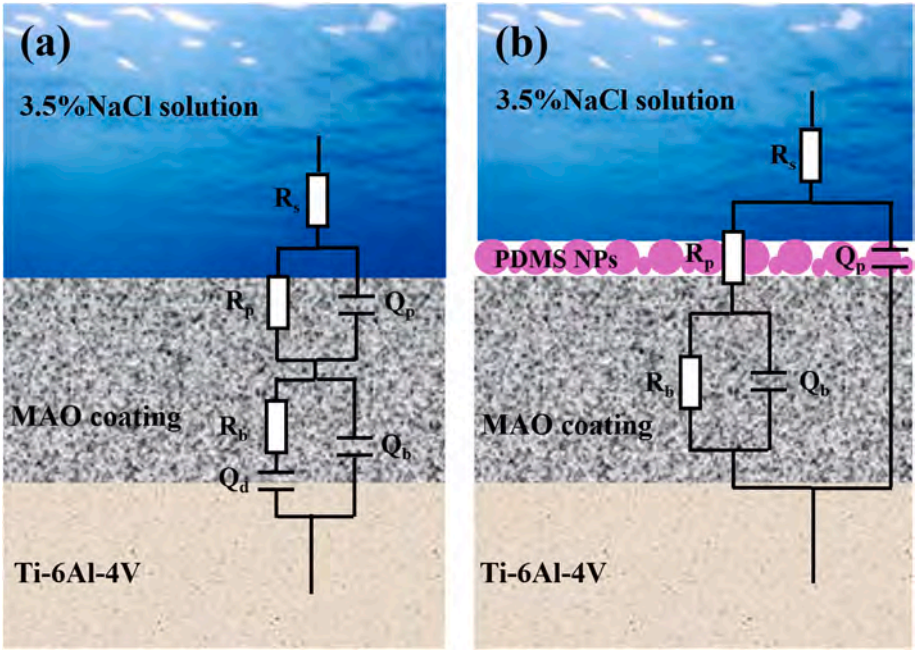

Fig. 11. Equivalent circuits to fit the EIS data.

MAO/PDMS is close to 90° in the high-frequency region (dense capacitance characteristics). The nanoparticles on the MAO coating after vapor deposition show improved densification of the MAO porous layer and provide a stronger barrier against corrosive media.

Coating porosity is an important indicator for describing the corrosion resistance of the coating, and for the effect of PDMS nanoparticles on the porosity of MAO/PDMS coating, it can be characterized by the following mathematical expression [55]:

$$P = \frac{R_{ps}}{R_p} \times 10^{-(\Delta E_{corr}/\beta_a)} \quad (4)$$

where P is the porosity of the MAO/PDMS superhydrophobic coating, R_{ps} is the polarization impedance of MAO-Ti, R_p is the polarization impedance of MAO/PDMS, $\Delta E_{corr}$is the potential difference between MAO-Ti and MAO/PDMS, and β_a is the anodic Tafel slope. The porosity of its MAO/PDMS superhydrophobic coating was 0.16 %, indicating that the PDMS nanoparticles clogged the microarc oxidation pores, leading to a smaller corrosion reaction area, hindering the formation of occlusion cells, slowing down the occurrence of localized corrosion, and greatly reducing the corrosion rate.

An equivalent circuit is proposed to fit the impedance data, as shown in Fig. 11. The equivalent circuit consists of the solution resistance (R_s), external porous layer resistance (R_p), internal dense layer resistance (R_d), external porous layer capacitance (Q_p) and internal dense layer capacitance (Q_d). In this case, the Q_b capacitive element is connected in series with the R_d resistive element in order to demonstrate diffusive corrosion after passing through the oxide layer [51]. The equivalent circuits of MAO-Ti and MAO/PDMS change from the Voigt structure to a trapezoidal structure due to the discharge micropores in MAO-Ti, which allow the corrosive fluid to penetrate to the coating/substrate interface, leading to diffusion-controlled corrosion. However, MAO/PDMS has higher penetration resistance due to the chemical inertness of the porous layer, leading to the suppressed diffusion control and a shift from diffusion-controlled dominance to interfacial reaction-controlled dominance. The impedance fitting parameters obtained by the Zview software are listed in Table 2. The internal dense layer resistance of MAO-Ti is larger than the external porous layer resistance, indicating that the corrosion resistance after MAO is dominated by the dense layer. Compared with MAO-Ti, no diffusion occurs in MAO/PDMS, and both the porous layer resistance and dense layer resistance are larger than those of MAO-Ti, and the corresponding porous layer capacitance and dense layer capacitance decrease. Therefore, the original rough microbumps of MAO and the low surface energy substance of PDMS NPs together improve the ability of the coating to capture air to produce the superhydrophobic properties, and MAO/PDMS has better corrosion resistance.

The durable corrosion resistance stability of each coating was characterized by salt spray exposure, in which the coatings were treated with continuous spraying in a salt spray chamber (5 wt% NaCl solution, 35 °C). Macroscopic photographs of the coatings at different time intervals are shown in Fig. 12. The MAO/PDMS superhydrophobic coating (Fig. 12(a)) showed a localized hydrophobic failure on day 3, with the hydrophobic failure region being the first one to occur at the circular holes, which was due to the fact that the punched holes were not covered by PDMS nanoparticles and there were defects on the surface, where the corrosive media were the first ones to pitting at the location, triggering the Wenzel state transition. Partial salt buildup can be observed on the surface, and with the extension of the test time, the area of its hydrophobic failure region slowly expands, and the phenomenon of salt buildup on the surface becomes more and more serious, and the phenomenon of salt buildup and hydrophobic failure region slowly appear on the edges of the styles on the 15th day. This is due to the contact of the coating with corrosive media, resulting in part of the hydrophobic functional group failure. Fig. 12(c)(e) shows the SEM images and

Table 2
Electrochemical impedance parameters from Nyquist plots.

Samples	R_s	Q_p	n_p	R_p	Q_b	n_b	R_b	Q_d	n_d
MAO-Ti	18.75	9.17E−7	0.76	253.2	1.28E−5	0.64	9567	1.96E−5	0.63
MAO/PDMS	301.2	1.11E−9	0.95	4.43E+5	7.15E−9	0.49	3.95E+7		

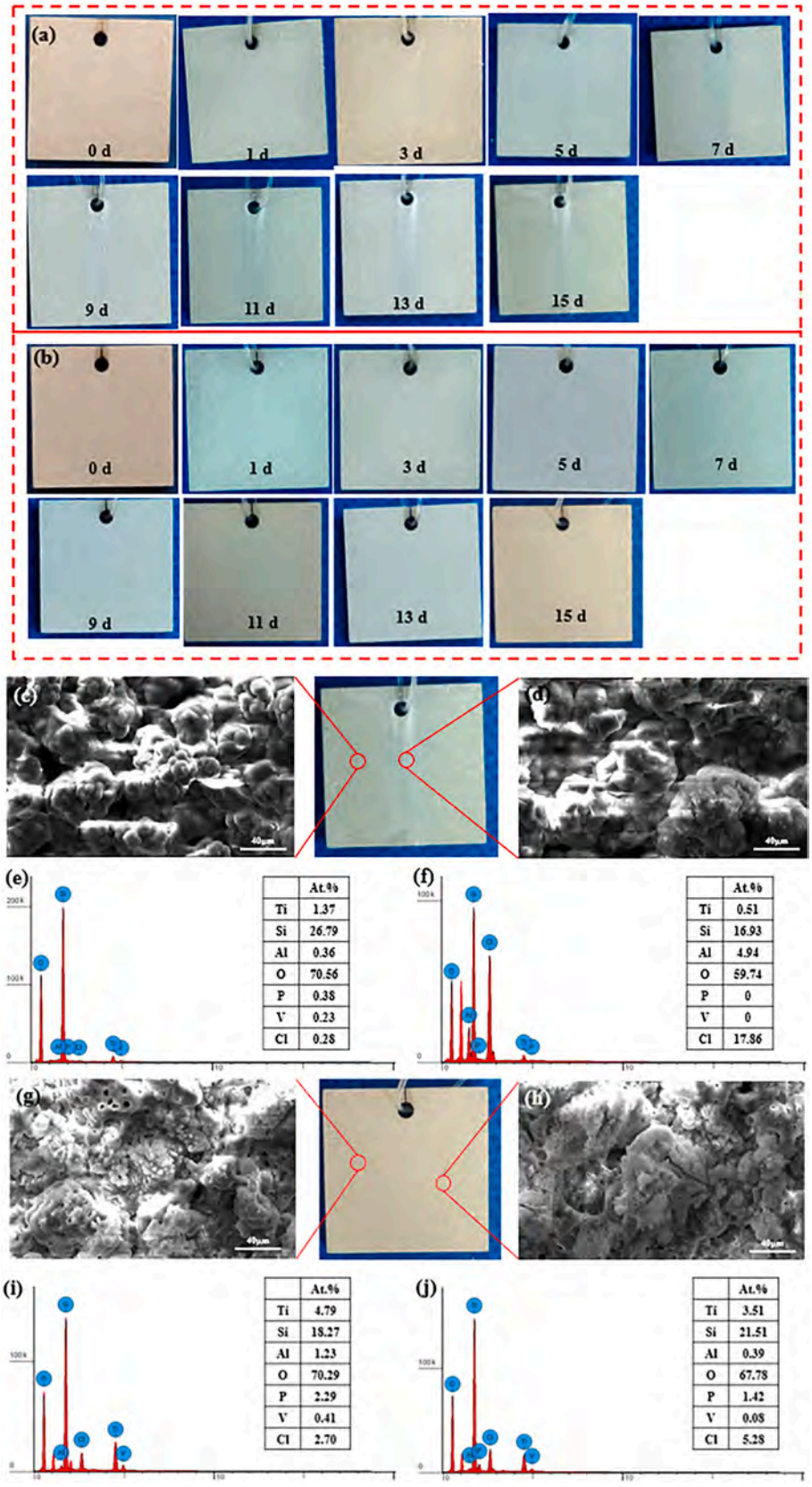

	At.%
Ti	1.37
Si	26.79
Al	0.36
O	70.56
P	0.38
V	0.23
Cl	0.28

	At.%
Ti	0.51
Si	16.93
Al	4.94
O	59.74
P	0
V	0
Cl	17.86

	At.%
Ti	4.79
Si	18.27
Al	1.23
O	70.29
P	2.29
V	0.41
Cl	2.70

	At.%
Ti	3.51
Si	21.51
Al	0.39
O	67.78
P	1.42
V	0.08
Cl	5.28

Fig. 12. Salt spray test photos of (a) MAO/PDMS coating and (b) MAO-Ti coating; surface micromorphology (c, d) and EDS composition (e, f) of MAO/PDMS samples after 15 days of salt spray corrosion; Surface micromorphology (g, h) and EDS composition (i, j) of MAO/PDMS samples after 15 days of salt spray corrosion.

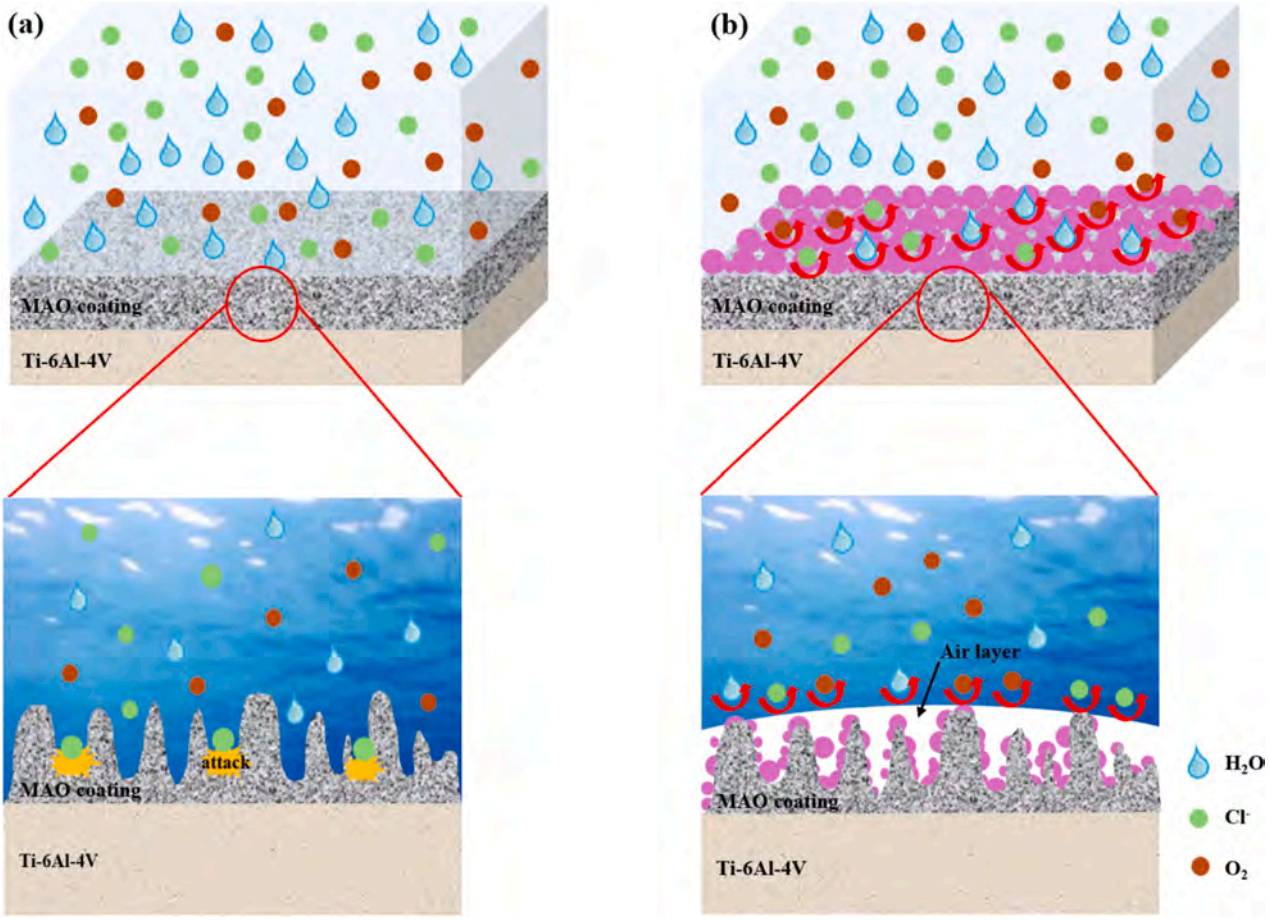

Fig. 13. Schematic corrosion mechanism of (a) MAO-Ti and (b) MAO/PDMS.

compositional composition of the hydrophobic region of the MAO/PDMS superhydrophobic coating. The hydrophobic region has less surface salt coverage, and elemental surface scanning of this region shows that the percentage of surface Cl ions is only 0.28 %, however, the hydrophobic failure region has a high percentage of 17.86 % due to more salt coverage, and elemental surface scanning of this region shows that the percentage of surface Cl ions is as high as 17.86 % (Fig. 12(d)(f)). Due to the large number of hydrophilic groups on the surface of the MAO-Ti coating, the droplets on the surface instantly nucleate and grow to extend to the whole sample when the salt spray contacts the sample, and the corrosive medium can reach the substrate preferentially through the holes and cracks on the surface of the coating and pitting corrosion occurs with the substrate. A small number of NaCl crystals can be observed in the microscopic morphology (Fig. 12(g)(h)), and the elemental surface scanning of this region reveals that its Cl ion content reaches 2.70 % and 5.28 %, respectively. This shows that the MAO/PDMS coating has excellent long-term stability and corrosion resistance.

3.6. Anticorrosion mechanism

Fig. 13 shows the corrosion protection mechanism. In MAO-Ti, there is a metallurgical bond between the MAO coating and the titanium alloy substrate. The MAO coating consists of a porous layer and a dense layer, and the porous layer provides limited corrosion resistance for the substrate, while the corrosion resistance of the MAO coating is mainly provided by the dense layer. However, MAO inevitably produces micropores and microcracks, and Cl^- ions can penetrate the coating to reach the substrate, leading to metal lattice amorphization [16]. According to our results, MAO/PDMS has better corrosion protection than MAO-Ti. The MAO coating provides basic protection for the substrate, and the superhydrophobic coating inhibits the penetration of corrosive media. Its rough structure and low surface energy produce an air layer that produces the synergistic effects of physical isolation and chemical inertness, which significantly inhibit the charge transfer and electrolyte diffusion of the corrosion reaction.

3.7. Friction experiment

In addition, in order to investigate the friction performance of the MAO/PDMS samples, friction experiments were carried out on the MAO-Ti samples and the MAO/PDMS samples.G10 bearing steel balls were used as the friction vice and loaded with a force of 0.3 N. Friction experiments were carried out on the two samples under no-lubrication conditions on the ball-and-disk friction tester at room temperature (23 °C–26 °C). The experimental results show that the friction performance of MAO-Ti is superior to that of MAO/PDMS, and the results of friction coefficients are displayed in Fig. 14(a)(b). Due to the attachment of PDMS nanoparticles on the surface of MAO/PDMS, the PDMS nanoparticles are mainly composed of PDMS debris and SiO_2 nanoparticles, which form high-resistance abrasive debris clusters and increase shear resistance, and the hard SiO_2 nanoparticles and soft PDMS debris are prone to trigger stress concentration and accelerate the adhesion failure. In addition, the surface roughness of its MAO/PDMS is higher compared to that of MAO-Ti, so that the average friction coefficient of MAO/PDMS is higher than that of MAO-Ti. Fig. 14(c) and (d) show the 3D surface profiles of MAO-Ti and MAO/PDMS, respectively, and the results show that the width of the abrasion marks of MAO/PDMS is larger than that of MAO-Ti. However, the surface of MAO/PDMS has a flatter abrasion mark surface with less flaking due to the presence of a large number of hard SiO_2 nanoparticles.

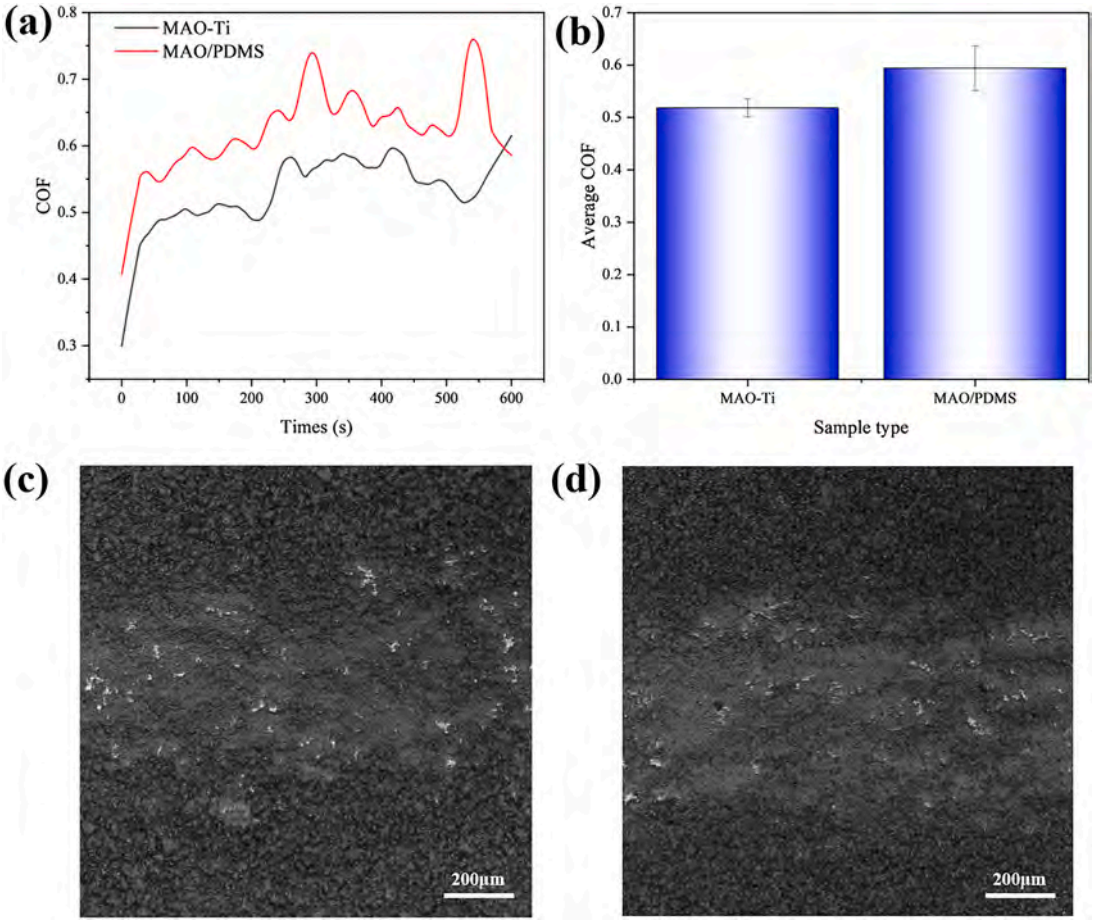

Fig. 14. (a, b) Average COF and instantaneous variation of COF for three samples under dry friction conditions; Surface wear morphology of (c) MAO-Ti, (d) MAO/PDMS.

4. Conclusions

MAO and PDMS layers are prepared by micro-arc oxidation and chemical vapor deposition on the Ti6Al4V titanium alloy to produce superhydrophobicity and improve the corrosion resistance and durability. The dual coating showing a surface angle of 166.2° has excellent water repellency and self-cleaning properties. After the tape stripping experiments, the coating still shows a wetting angle of >150°, and hydrophobicity is better after friction tests. The corrosion resistance is enhanced due to the synergistic effects rendered by the MAO coating and superhydrophobicity. The self-corrosion current density of MAO/PDMS rises by three orders of magnitude, and the impedance modulus rises by two orders of magnitude compared to MAO-Ti. The coating retains the mechanical stability during abrasion tests and self-cleaning ability, boding well for applications under harsh conditions. In the friction experiments, the friction coefficient of MAO/PDMS is the largest, which is due to the roughness of MAO-Ti is smaller than that of MAO/PDMS, and the PDMS nanoparticles produced by vapor deposition consist of SiO_2 nanoparticles and residual PDMS, which are soft and hard interacting with each other, increasing the shear resistance and accelerating the adhesive wear.

CRediT authorship contribution statement

Yinghe Ma: Investigation, Methodology, Writing – original draft, Writing – review & editing. **Yonghui Hu:** Conceptualization, Methodology, Writing – original draft, Writing – review & editing. **Zhen Yu:** Conceptualization, Investigation, Writing – review & editing. **Zhihui Cai:** Conceptualization, Resources, Supervision. **Wenjian Zheng:** Resources, Supervision, Visualization. **Jianguo Yang:** Funding acquisition, Supervision, Writing – review & editing. **Paul K. Chu:** Funding acquisition, Supervision, Writing – review & editing.

Declaration of competing interest

No potential conflict of interest was reported by the author(s).

Acknowledgments

The paper was funded by the National Natural Science Foundation of China (No. 52375391), Wenzhou Basic Scientific Research Project (grant number G2023065) and City University of Hong Kong Donation Research Grants (DON-RMG 9229021 and 9220061).

Data availability

The data that has been used is confidential.

References

[1] X. Yang, F.H. Wang, W.L. Wang, S.F. Liu, Y.Q. Chen, H.-P. Tang, Comparison of two-step surface treatment on surface roughness and corrosion resistance of TC4 alloy parts prepared by SLM and SEBM, J. Alloys Compd. 921 (2022) 165929, https://doi.org/10.1016/j.jallcom.2022.165929.
[2] F. Gao, Z. Sun, S. Yang, et al., Stress corrosion characteristics of electron beam welded titanium alloys joints in NaCl solution, Mater Charact 192 (2022) 112126, https://doi.org/10.1016/j.matchar.2022.112126.
[3] G. Xin, C. Wu, H. Cao, W. Liu, B. Li, Y. Huang, Y. Rong, G. Zhang, Superhydrophobic TC4 alloy surface fabricated by laser micro-scanning to reduce

adhesion and drag resistance, Surf. Coat. Technol. 391 (2020) 125707, https://doi.org/10.1016/j.surfcoat.2020.125707.
[4] M. Hagiwara, S. Emura, Blended elemental P/M synthesis and property evaluation of Ti-1100 alloy, Mater. Sci. Eng. A 352 (2003) 85–92, https://doi.org/10.1016/S0921-5093(02)00897-3.
[5] C. Liu, S. Tong, Y. Yue, H. Wang, J. Song, Y. Li, Q. Wang, Z. Wang, Laser-based fabrication of superwetting titanium alloy with enhanced corrosion and erosion-corrosion resistance, Colloids Surf., A 688 (2024) 133648, https://doi.org/10.1016/j.colsurfa.2024.133648.
[6] X.J. Cui, X.Z. Lin, C.H. Liu, R.S. Yang, X.W. Zheng, M. Gong, Fabrication and corrosion resistance of a hydrophobic micro-arc oxidation coating on AZ31 Mg alloy, Corros. Sci. 90 (2015) 402–412, https://doi.org/10.1016/j.corsci.2014.10.041.
[7] A. Gao, R.Q. Hang, L. Bai, B. Tang, P.K. Chu, Electrochemical surface engineering of titanium-based alloys for biomedical application, Electrochim. Acta 271 (2018) 699–718, https://doi.org/10.1016/j.electacta.2018.03.180.
[8] K. Korkmaz, The effect of Micro-arc oxidation treatment on the microstructure and properties of open cell Ti6Al4V alloy foams, Surf. Coat. Technol. 272 (2015) 72–78, https://doi.org/10.1016/j.surfcoat.2015.04.022.
[9] K. Ling, Q. Mo, X. Lv, G. Qin, W. Yang, L. Li, W. Li, Growth characteristics and corrosion resistance of micro-arc oxidation coating on Al-Mg composite plate, Vacuum 195 (2022) 110640, https://doi.org/10.1016/j.vacuum.2021.110640.
[10] Y. Wang, Q. Peng, G. Wu, J. Yao, Y. Yin, L. Li, Y. Zheng, C. Wen, Effect of auxiliary laser irradiation on characteristics and properties of micro-arc oxidation coating on Ti6Al4V alloy, Ceram. Int. 50 (2024) 19412–19423, https://doi.org/10.1016/j.ceramint.2024.03.045.
[11] G. Wu, Y. Yin, S. Zhang, Y. Wang, Y. Xiang, L. Li, J. Yao, Effect of laser texturing on the antiwear properties of micro-arc oxidation coating formed on Ti-6Al-4V, Surf. Coat. Technol. 453 (2023) 129114, https://doi.org/10.1016/j.surfcoat.2022.129114.
[12] G. Li, F. Ma, P. Liu, S. Qi, W. Li, K. Zhang, X. Chen, Review of micro-arc oxidation of titanium alloys: mechanism, properties and applications, J. Alloys Compd. 948 (2023) 169773, https://doi.org/10.1016/j.jallcom.2023.169773.
[13] X. Chen, D. Liao, X. Jiang, D. Zhang, T. Shi, Effect of tungsten doping on the performance of MAO coatings on a Ti6Al4V drill pipe, Surf. Innovations 8 (2020) 279–286, https://doi.org/10.1680/jsuin.20.00002.
[14] G. Li, Y. Wang, L. Qiao, R. Zhao, S. Zhang, R. Zhang, C. Chen, X. Li, Y. Zhao, Preparation and formation mechanism of copper incorporated micro-arc oxidation coatings developed on Ti-6Al-4V alloys, Surf. Coat. Technol. 375 (2019) 74–85, https://doi.org/10.1016/j.surfcoat.2019.06.096.
[15] Y. Ma, P. Wu, J. Mei, Z. Yu, J. Yang, Y. He, H. Li, C. Lv, S. Ren, J. Xu, Z. Cai, P. K. Chu, Effects of micro-arc oxidation surface treatment on the corrosion resistance of Ti-6Al-4V electron-beam-welded joints, Metals 13 (7) (2023) 1161, https://doi.org/10.3390/met13071161.
[16] L. Wu, Q. Ye, K. Zhang, X. Guo, J. Li, Y. Chen, F. Fang, H. Chang, Fabrication of hydrophobic corrosion-resistant microarc oxidation titanium alloy through pore-sealing treatment with secondary growth of ZIF-8 seed crystals, Surf. Coat. Technol. 501 (2025) 131898, https://doi.org/10.1016/j.surfcoat.2025.131898.
[17] X. Qi, H. Gao, Y. He, X. Su, R. Song, Microstructure and properties of a MAO/PA/MoS2 composite coating formed on 6063 aluminum alloy by micro arc oxidation, Surf. Coat. Technol. 484 (2024) 130836, https://doi.org/10.1016/j.surfcoat.2024.130836.
[18] D. Yue, X. Jiang, H. Yu, D. Sun, In-situ fabricated hierarchical nanostructure on titanium alloy as highly stable and durable super-lubricated surface for anti-biofouling in marine engineering, Chem. Eng. J. 463 (2023) 142389, https://doi.org/10.1016/j.cej.2023.142389.
[19] X. Zhan, W. Shang, Y. Wen, Y. Li, M. Ma, Preparation and corrosion resistance of a three-layer composite coatings on the Mg alloy, J. Alloys Compd. 774 (2019) 522–531, https://doi.org/10.1016/j.jallcom.2018.10.059.
[20] S. Wang, Y. Wang, G. Cao, J. Chen, Y. Zou, B. Yang, J. Ouyang, D. Jia, Y. Zhou, Highly reliable double-layer coatings on magnesium alloy surfaces for robust superhydrophobicity, chemical durability and electrical property, Ceram. Int. 47 (2021) 35037–35047, https://doi.org/10.1016/j.ceramint.2021.09.045.
[21] H. Li, Z. Wang, Corrosion behavior and incorporation mechanism of Y2O3-TiO2 composite coatings fabricated on TC4 titanium alloy by plasma electrolytic oxidation, Chem. Phys. Lett. 841 (2024) 141170, https://doi.org/10.1016/j.cplett.2024.141170.
[22] Y. Wang, D. Lu, G. Wu, K. Chen, H. Wu, Q. Zhang, et al., Effect of laser surface remelting pretreatment with different energy density on MAO bioceramic coating, Surf. Coat. Technol. 393 (2020) 125815, https://doi.org/10.1016/j.surfcoat.2020.125815.
[23] X.W. Chen, M.L. Li, D.F. Zhang, L.P. Cai, P. Ren, J. Hu, D.D. Liao, Corrosion resistance of MoS2-modified titanium alloy micro-arc oxidation coating, Surf. Coat. Technol. 433 (2022) 128127, https://doi.org/10.1016/j.surfcoat.2022.128127.
[24] S. Wang, Z. Zhang, W. Qian, Y. Yu, Y. Chen, Q. Zhao, Y. Zhang, H. Li, Y. Zhao, Enhancing corrosion resistance of AZ91D alloy through yttria-stabilized tetragonal zirconia (YSTZ)/MgO repaired ceramic coating with improved embrittlement cracking, Corros. Sci. 225 (2023) 111634, https://doi.org/10.1016/j.corsci.2023.111634.
[25] S. Buyuksungur, A.C. Parau, M. Dinu, I. Pana, C. Vitelaru, J. Schmidt, T.E. Tanir, V. Hasirci, A. Vladescu, N. Hasirci, Variations of chemical, physical, mechanical properties, and biological and antimicrobial effectiveness of Ti alloys by coating with Ca-P doped with different amounts of Zn via micro-arc oxidation (MAO) technique, Ceram. Int. 50 (19) (2024) 37096–37110, https://doi.org/10.1016/j.ceramint.2024.07.100.
[26] J. Wei, B. Li, N. Tian, J. Zhang, W. Liang, J. Zhang, Scalable robust superamphiphobic coatings enabled by self-similar structure, protective micro-skeleton, and adhesive for practical anti-icing of high-voltage transmission tower, Adv. Funct. Mater. 32 (2022), https://doi.org/10.1002/adfm.202206014.
[27] T. Zhu, Y. Cheng, J. Huang, J. Xiong, M. Ge, J. Mao, Z. Liu, X. Dong, Z. Chen, Y. Lai, A transparent superhydrophobic coating with mechanochemical robustness for anti-icing, photocatalysis and self-cleaning, Chem. Eng. J. 399 (2020), https://doi.org/10.1016/j.cej.2020.125746.
[28] Y. Zhang, X. Fan, W. Zhu, X. Li, M. Cai, Y. Huang, C. He, L. Zhang, B. Lin, M. Zhu, Probing photothermal superhydrophobic behaviors of graphene&SiO2 hybrid coating for anti-freeze application, Ceram. Int. 49 (2023) 33020–33028, https://doi.org/10.1016/j.ceramint.2023.08.001.
[29] R. Ji, C. Liu, J. Zhang, S. Zhang, L. Zhang, Y. Lian, Hydrophobicity and tribological properties of Al2O3/PTFE composite coating, Rare Metals 42 (11) (2018) 3870–3876, https://doi.org/10.1007/s12598-018-1149-0.
[30] X. Han, Z. You, J. Li, R. Ma, Y. Fan, A. Du, X. Zhao, M. Yang, Study on the performance of self-healing superhydrophobic coating on micro-arc oxidized surface with PDMS/PCL@F-SiO2, Surf. Coat. Technol. 494 (2024) 131498, https://doi.org/10.1016/j.surfcoat.2024.131498.
[31] Y. Zou, Y. Wang, S. Xu, T. Jin, D. Wei, J. Ouyang, D. Jia, Y. Zhou, Superhydrophobic double-layer coating for efficient heat dissipation and corrosion protection, Chem. Eng. J. 362 (2019) 638–649, https://doi.org/10.1016/j.cej.2019.01.086.
[32] B. Zhang, G. Yang, W. Xu, J. Duan, B. Hou, Hybrid superamphiphobic anti-corrosion coating with integrated functionalities of liquid repellency, self-cleaning, and anti-icing, J. Mater. Sci. Technol. 184 (2024) 256–268, https://doi.org/10.1016/j.jmst.2023.10.042.
[33] G. Xu, P. Liu, A. Liu, C. Zhang, G. Zhang, Q. Wu, H. Lu, Mechanically stable superhydrophobic surfaces constructed by laser surface texturing and micro-arc oxidation of TC4 alloy prepared based on SLM, Mater. Chem. Phys. 325 (2024) 129791, https://doi.org/10.1016/j.matchemphys.2024.129791.
[34] S. Wang, Y. Wang, Y. Zou, G. Chen, J. Ouyang, D. Jia, Y. Zhou, Scalable-manufactured superhydrophobic multilayer nanocomposite coating with mechanochemical robustness and high-temperature endurance, ACS Appl. Mater. Interfaces 12 (2020) 31, https://doi.org/10.1021/acsami.0c10539.
[35] Y. Ye, Z. Kang, F. Wang, Y. Long, T. Guo, D. Chen, J. Kong, L. Xu, Achieving hierarchical structure with superhydrophobicity and enhanced anti-corrosion via electrochemical etching and chemical vapor deposition, Appl. Surf. Sci. 610 (2023) 155362, https://doi.org/10.1016/j.apsusc.2022.155362.
[36] Y. Zhang, X. Fan, X. Li, Z. Zhang, Y. Zhang, Z. Chen, S. Ge, Y. Wang, M. Zhu, Microstructure design of black ceramic composite surface towards photothermal superhydrophobic anti-icing, Chem. Eng. J. 498 (2024) 155101, https://doi.org/10.1016/j.cej.2024.155101.
[37] S.M.A. Shibli, F. Chacko, Development of nano TiO2-incorporated phosphate coatings on hot dip zinc surface for good paintability and corrosion resistance, Appl. Surf. Sci. 257 (2011) 3111–3117, https://doi.org/10.1016/j.apsusc.2010.10.125.
[38] V.S. Kathavate, P.P. Deshpande, Role of nano TiO2 and nano ZnO particles on enhancing the electrochemical and mechanical properties of electrochemically deposited phosphate coatings, Surf. Coat. Technol. 394 (2020) 125902, https://doi.org/10.1016/j.surfcoat.2020.125902.
[39] J. Genzer, K. Efimenko, Creating long-lived superhydrophobic polymer surfaces through mechanically assembled monolayers, Science 290 (2000) 2130–2133, https://doi.org/10.1126/science.290.5499.2130.
[40] A.B.D. Cassie, S. Baxter, Wettability of porous surfaces, Trans. Faraday Soc. 40 (1944) 546–551, https://doi.org/10.1039/TF9444000546.
[41] Y. Chen, H. Liu, L. Yu, Q. Duan, Z. Ji, L. Chen, Superhydrophobic modification on starch film using PDMS and ball-milled MMT coating, ACS Sustain. Chem. Eng. 8 (2020) 10423–10430, https://doi.org/10.1021/acssuschemeng.0c02077.
[42] Q. Wu, J. Xu, N. Tu, B. Xue, J. Chen, H. Lu, Preparation of mechanically durable superhydrophobic aluminum surfaces by LST/MAO and chemical modification, Colloids Surf. A Physicochem. Eng. Asp. 689 (2024) 133722, https://doi.org/10.1016/j.colsurfa.2024.133722.
[43] J.M. Wheeler, C.A. Collier, J.M. Paillard, J.A. Curran, Evaluation of micromechanical behaviour of plasma electrolytic oxidation (PEO) coatings on Ti–6Al–4V, Surf. Coat. Technol. 204 (2010) 3399–3409, https://doi.org/10.1016/j.surfcoat.2010.04.006.
[44] Y.M. Wang, B.L. Jiang, T.Q. Lei, L.X. Guo, Microarc oxidation coatings formed on Ti6Al4V in Na_2SiO_3 system solution: microstructure, mechanical and tribological properties, Surf. Coat. Technol. 201 (2006) 82–89, https://doi.org/10.1016/j.surfcoat.2005.10.044.
[45] M. Long, S. Peng, X. Yang, W. Deng, N. Wen, K. Miao, G. Chen, X. Miao, W. Deng, One-step fabrication of non-fluorinated transparent super-repellent surfaces with tunable wettability functioning in both air and oil, ACS Appl. Mater. Interfaces 9 (2017) 15857–15867, https://doi.org/10.1021/acsami.7b01926.
[46] W. Sun, L. Wang, Z. Yang, S. Li, T. Wu, G. Liu, Fabrication of polydimethylsiloxane-derived superhydrophobic surface on aluminium via chemical vapour deposition technique for corrosion protection, Corros. Sci. 128 (2017) 176–185, https://doi.org/10.1016/j.corsci.2017.09.005.
[47] X. Liu, Y. Wang, Z. Chen, K. Ben, Z. Guan, A self-modification approach toward transparent superhydrophobic glass for rainproofing and superhydrophobic fiberglass mesh for oil-water separation, Appl. Surf. Sci. 360 (2016) 789–797, https://doi.org/10.1016/j.apsusc.2015.11.069.
[48] J. Wang, G. Li, Z. Zhang, Q. Huang, B. Niu, Y. Zhang, D. Long, Detailed insights of polydimethylsiloxane (PDMS) degradation mechanism via ReaxFF MD and

experiments, Chem. Eng. J. 488 (2024) 150728, https://doi.org/10.1016/j.cej.2024.150728.
[49] J. Ou, W. Hu, M. Xue, F. Wang, W. Li, Superhydrophobic surfaces on light alloy substrates fabricated by a versatile process and their corrosion protection, ACS Appl. Mater. Interfaces 5 (2013) 3101–3107, https://doi.org/10.1021/am4000134.
[50] S. Jiang, W. Li, J. Liu, J. Jiang, Z. Zhang, W. Shang, N. Peng, Y. Wen, ZnO@ZIF-8 core-shell structure nanorods superhydrophobic coating on magnesium alloy with corrosion resistance and self-cleaning, J. Magnesium Alloys 11 (9) (2023) 3287–3301, https://doi.org/10.1016/j.jma.2022.01.014.
[51] X. Yin, P. Mu, Q. Wang, J. Li, Superhydrophobic ZIF-8-based dual-layer coating for enhanced corrosion protection of Mg alloy, ACS Appl. Mater. Interfaces 12 (31) (2020) 35453–35463, https://doi.org/10.1021/acsami.0c09497.
[52] Y.M. Shixiong Hea, Hong Yeb, Xiangdong Liua, Zuoyong Doua, Qingdong Xua, Haijun Wanga, Pengcheng Zhang, Ceramic oxide coating formed on beryllium by micro-arc oxidation, Corros. Sci. 122 (2017) 108–117, https://doi.org/10.1016/j.corsci.2017.04.001.
[53] M. Fazel, H.R. Salimijazi, M.A. Golozar, M.R. Garsivaz Jazi, A comparison of corrosion, tribocorrosion and electrochemical impedance properties of pure Ti and Ti6Al4V alloy treated by micro-arc oxidation process, Appl. Surf. Sci. 324 (2015) 751–756, https://doi.org/10.1016/j.apsusc.2014.11.030.
[54] X. Wang, C. Jing, Y. Chen, X. Wang, G. Zhao, X. Zhang, L. Wu, X. Liu, B. Dong, Y. Zhang, Active corrosion protection of super-hydrophobic corrosion inhibitor intercalated Mg–Al layered double hydroxide coating on AZ31 magnesium alloy, J. Magnesium Alloys. 8 (1) (2020) 291–300, https://doi.org/10.1016/j.jma.2019.11.011.
[55] V.F.C. Lins, G.F.A. Reis, C.R. Araujo, T. Matencio, Electrochemical impedance spectros copy and linear polarization applied to evaluation of porosity of phosphate conversion coatings on electrogalvanized steels, Appl. Surf. Sci. 253 (2006) 2875–2884, https://doi.org/10.1016/j.apsusc.2006.06.030.